MNRAS **537**, 293–305 (2025) Advance Access publication 2025 January 8

Testing disc reprocessing models for AGN optical variability by comparison of X-ray and optical power spectra of NGC 4395

M. W. J. Beard, 1* I. M. McHardy, 1 K. Horne, 2 E. M. Cackett, 3 F. Vincentelli, 1,4,5 J. V. Hernández Santisteban, J. Miller, V. S. Dhillon, J. H. Knapen, J. S. P. Littlefair, D. Kynoch, 1 E. Breedt ¹⁰. Y. Shen⁸ and J. Gelbord⁹

Accepted 2025 January 3. Received 2025 January 2; in original form 2024 October 13

ABSTRACT

It is generally thought that active galactic nucleus (AGN) optical variability is produced, at least in part, by reprocessing of central X-rays by a surrounding accretion disc, resulting in wavelength-dependent lags between bands. Any good model of AGN optical variability should explain not only these lags, but also the overall pattern of variability as quantified by the power spectral density (PSD). Here, we present ~daily g'-band monitoring of the low-mass AGN NGC 4395 over 3 yr. Together with previous Transiting Exoplanet Survey Satellite (TESS) and Gran Telescopio Canarias (GTC)/HiPERCAM observations, we produce an optical PSD covering an unprecedented frequency range of ~seven decades allowing excellent determination of PSD parameters. The PSD is well fitted by a bending power law with low-frequency slope $\alpha_L = 1.0 \pm 0.2$, high-frequency slope $2.1^{+0.2}_{-0.4}$, and bend time-scale $3.0_{-1.7}^{+6.6}$ d. This time-scale is close to that derived previously from a damped random walk (DRW) model fitted to just the TESS observations, although α_L is too steep to be consistent with a DRW. We compare the observed PSD with one made from light curves synthesized assuming reprocessing of X-rays, as observed by XMM–Newton and Swift, in a disc defined by the observed lags. The simulated PSD is also well described by a bending power law but with a bend two decades higher in frequency. We conclude that the large-amplitude optical variations seen on long time-scales are not due to disc reprocessing but require a second source of variability whose origin is unknown but could be propagating disc accretion rate variations.

Key words: galaxies: active – galaxies: individual: NGC 4395 – X-rays: galaxies.

1 INTRODUCTION

Active galactic nuclei (AGNs) have long been observed to emit Xray continua that vary rapidly and non-periodically (e.g. Lawrence et al. 1987; McHardy & Czerny 1987), consistent with the idea that the X-ray emission originates from a compact region within a few Schwarzschild radii of the central black hole. X-ray variability is often characterized by the power spectral density (PSD) of the light curve. From early European X-ray Observatory Satellite (EXOSAT) observations it was shown that AGN X-ray PSDs are well described by bending power laws, $P(\nu) \propto \nu^{-\alpha}$, with $\alpha \sim 2$ at high frequencies (> 10^{-5} Hz), flattening to $\alpha \sim 1$ below a bend frequency ν_B (M^cHardy 1988). By comparison with the PSDs of galactic X-ray

The origin of short-time-scale (hours/days) optical variability in AGN was a mystery for many years. However, many observations over the last two decades have shown a strong correlation between X-ray and optical variations, with the optical lagging behind the X-rays. This correlation strongly suggests that at least part of the optical variability is driven by reprocessing of X-rays. There is good evidence that the accretion disc, the broad-line region (BLR) gas and quite possibly also a disc wind act as reprocessors although there is still considerable discussion as to their relative importance, e.g. Korista & Goad (2001, 2019), Uttley et al. (2003), Cackett, Horne &

¹School of Physics and Astronomy, University of Southampton, University Road, Southampton SO17 1BJ, UK

²School of Physics and Astronomy, University of St Andrews, North Haugh, St Andrews KY16 9SS, UK

³Department of Physics and Astronomy, Wayne State University, 666 W. Hancock Street, Detroit, MI 48201, USA

⁴Departamento de Astrofísica, Universidad de La Laguna, E-38206 La Laguna, Spain

⁵Instituto de Astrofísica de Canarias, Vía Láctea S/N, E-38205 La Laguna, Spain

⁶Department of Physics and Astronomy, University of Sheffield, Sheffield S3 7RH, UK

⁷Institute of Astronomy, University of Cambridge, Madingley Road, Cambridge, CB3 0HE, UK

⁸Department of Astronomy, University of Illinois at Urbana-Champaign, 1002 W. Green Street, Urbana, IL 61801, USA

⁹Spectral Sciences Inc, 4 Fourth Avenue, Burlington, MA 01803, USA

binary systems (e.g. Nolan et al. 1981) it was proposed that the bend time-scale was proportional to the black hole mass (McHardy 1988), a proposition which was supported by many subsequent observations (e.g. Nandra & Papadakis 2001; Uttley, McHardy & Papadakis 2002; McHardy et al. 2004, 2006; Ponti et al. 2012; Tortosa et al. 2023; Serafinelli et al. 2024).

^{*} E-mail: mb15g14@soton.ac.uk

Winkler (2007), Arévalo et al. (2008), Breedt et al. (2009, 2010), McHardy et al. (2014, 2016), Shappee et al. (2014), Edelson et al. (2015, 2019), Cackett et al. (2018, 2020), McHardy et al. (2018), Netzer (2019), Kara et al. (2021), Vincentelli et al. (2021, 2022), Hagen, Done & Edelson (2024), and many others.

If the optical variability of AGNs is mostly due to reprocessing of X-rays, then the characteristic signature of the X-ray variations, i.e. the shape of the X-ray PSD, should be present in the PSD of the optical variations. In particular, the optical PSD should be the product of the PSD of the X-ray variations with the square of the modulus of the response function of the reprocessing material (e.g. see Arévalo et al. 2009). Alternatively, the optical PSD can be produced by convolving the X-ray light curves with the response function and then calculating the PSD of the resulting reprocessed optical light curves. Comparison of an observed optical PSD with a model PSD based on reprocessing is therefore a powerful tool for testing whether the reprocessing model is correct and whether it explains all optical variability. This comparison can be carried out independently of measurement of an interband lag. However, if combined with measurement of a lag, or multiple interband lags, which constrain the response function, the test is stronger (Arévalo et al. 2009; Panagiotou et al. 2022; Hagen & Done 2023). Comparison of the optical and X-ray PSDs of one particularly well-studied AGN is the aim of this paper.

AGN optical PSDs have been studied previously by a number of previous authors. We discuss some of the main observations here. Czerny, Schwarzenberg-Czerny & Loska (1999) modelled the optical PSD of NGC 5548 with a broken power law, claiming a break at \sim 100 d. However, they did not take into account PSD distortions from red noise leak and irregular sampling so the time-scale uncertainty is unclear. Arévalo et al. (2009) measured the X-ray and optical power spectra of NGC 3783. They found that the X-ray PSD was described by a bending power law with a bend at ~ 3 d. However, the optical PSD continued rising as an unbending power law towards the longest time-scales covered (\sim 300 d). Thus, the X-ray power exceeded the optical power at high frequencies but vice-versa at low frequencies. Arévalo et al. (2009) also measured the lag of the X-rays by the optical B and V bands (\sim 6 d) and constructed response functions for a variety of reprocessing geometries to determine which one best reproduced the observed ratio of the optical to X-ray PSDs. Given the 6 d lag, no geometry could smooth the X-ray variations sufficiently to produce the observed optical variability, particularly at low frequencies.

Breedt et al. (2010) carried out a detailed X-ray and optical variability study of NGC 4051 using light curves of over 12 yr. They found that, while the X-ray PSD was well described by a bending power law (McHardy et al. 2004), the optical PSD was adequately described by an unbending power law of slope ~ 1.4 , intermediate between the high-frequency (~ 2) and low-frequency (~ 1.1) X-ray PSD slopes. This intermediate slope may have resulted from the optical data not being good enough to properly define a PSD bend.

Breedt (2010) calculated the optical PSDs of six more bright Seyfert 1 galaxies (NGC 3227, NGC 4593, NGC 5548, NGC 7469, Mrk79, Mrk110) and compared the optical PSDs with the X-ray PSDs derived by Summons (2007). The results were broadly similar to those of Arévalo et al. (2009) finding, in three cases (NGC 5548, NGC 4593, and Mrk 79), that the optical power exceeded the X-rays at low frequencies. Although bending power laws could be fitted to the optical PSDs, in no case were they a better fit than an unbending power law.

The optical data used by the above authors, although covering periods of more than a decade, were generally limited to groundbased observations once per night. Considerably improved sampling was provided by the *Kepler* (Borucki et al. 2010) and Transiting Exoplanet Survey Satellite (*TESS*) (Ricker et al. 2014) space observatories. *Kepler* observed selected areas continuously in white light with 30 min sampling for one or more periods of 3 months (quarters). *TESS* also has 30 min sampling with continuous observations of \sim 1 month in a broad red (600–1000 nm) observing band.

From *Kepler* data Mushotzky et al. (2011) measured the PSDs of four type 1 AGNs, finding unbending power law slopes between 2.6 and 3.3. Smith et al. (2018) found a similar single slope range for a sample of 21 type 1 AGNs although, for the 6 PSDs with the steepest high-frequency slopes (α_H) , bending power laws were a better fit. The bend time-scales (9 to 53 d) roughly scaled with mass. Smith et al. (2018) do not discuss the slopes below the bend (α_L) but visual inspection of their fig. 10 indicates $\alpha_L > 0$ in four AGNs and $\alpha_L \leq 0$ in two. Probably the highest signal-to-noise ratio (S/N) Kepler AGN PSD is that of Zw 229-15 (Edelson et al. 2014). They find a bending PSD with a very steep high-frequency slope (\sim 3.6) flattening, on time-scales > 5 d, to $\alpha_L \sim 2$. Unfortunately, there is no X-ray PSD available for comparison. Edelson et al. (2014) also found no evidence for rms/flux relationships or lognormal flux distributions, which are common in X-ray AGN light curves, and so they concluded that X-ray reprocessing did not drive the optical variability.

The PSD slopes from Mushotzky et al. (2011) are interesting because they are steeper than the value of 2 expected for the high-frequency PSD slope in the damped random walk (DRW) model which is commonly applied to AGN optical variations (e.g. Kelly, Bechtold & Siemiginowska 2009). The DRW PSD is also characterized by a low-frequency PSD slope of zero and a damping time-scale, τ , equivalent to the bend time-scale of a bending power law PSD, which Burke et al. (2021) have shown scales with mass from white dwarfs to AGNs. Using variants of the DRW model, Zu et al. (2013), Stone et al. (2022), and Yu et al. (2022), all suggest a steepening of the PSD slope at the highest frequencies, possibly indicating a second, high-frequency, bend time-scale.

Measurement of low-frequency PSD slopes in bending or breaking power law models is rare. However, Simm et al. (2016) using continuous-time autoregressive moving average (CARMA) models (Kelly et al. 2014), found slopes consistent with 1 in the PSDs derived from the Panoramic Survey Telescope and Rapid Response System (Pan-STARRS1) light curves of AGNs in the Cosmos–XMM field. Above the bend they found a range of slopes between 2 and 4. These low-frequency slopes again cast doubt on at least the simple version of DRW as the explanation of all AGN optical variability.

Of particular relevance to this paper, we note the results of Burke et al. (2020) on NGC 4395. They model *TESS* data with a DRW, finding a damping time-scale of 2.3 d. They also fit a broken power law to the PSD covering two decades in frequency from $\sim 3 \times 10^{-7}$ to $\sim 3 \times 10^{-5}$ Hz, finding $\alpha_H \sim 2$ and $\alpha_L \sim 0$. The damping time-scale is towards the bottom end of the time-scales covered by *TESS* and a major aim of this paper is to refine these results with larger frequency coverage.

Panagiotou et al. (2022), broadly following Arévalo et al. (2009) and Breedt et al. (2010), modelled together the multiband PSDs and lags of NGC 5548 using data from *Swift* (Edelson et al. 2015). Covering a slightly lower frequency band than *TESS*, and with reduced frequency range (\sim 1.5 decades), they found power law PSD slopes \sim 2. Unlike Arévalo et al. (2009) they concluded that X-ray disc reprocessing could adequately describe both the lags and the PSDs.

Although reprocessing of central X-rays provides a good explanation of short-term optical variability, there are longer term (months/years) variations in the optical light curves which often have no parallel in the X-ray band (e.g. Arévalo et al. 2008; Breedt et al. 2010). These variations may explain why, at the very lowest frequencies, the optical PSDs of AGNs often have more power than the X-ray PSDs. The origin of the long-time-scale variations is unknown but they may represent intrinsic variability of the quiescent accretion disc, perhaps as a result of inwardly propagating accretion rate variations (Arevalo & Uttley 2006). Such variability would occur not on the fast light-travel time-scales of reprocessing but on the much slower viscous time-scale. Slow moving temperature fluctuations, travelling both inward and outward in the disc, have recently been found by Neustadt & Kochanek (2022) and Stone & Shen (2023) from analysis of Swift ultraviolet (UV)/optical and Sloan Digital Sky Survey (SDSS) light curves, respectively. The physical origin of these fluctuations is not yet clear but they may be related to the non-reverberation signals seen by, for example Arévalo et al. (2008) and Breedt et al. (2010).

The situation, then, regarding how much of the optical variability of AGNs can be attributed to reprocessing of X-rays and, if so, reprocessing from what, is not yet entirely clear. Whether optical AGN PSDs can be explained easily by the disc reprocessing scenario is even less clear. To provide a strong test of the reprocessing scenario for PSDs there are a number of requirements. First, we require very good X-ray and optical light curves so that we can produce high S/N PSDs in both bands. Secondly, we require frequency coverage over a large range, at least four decades in X-rays, so that we can properly define the PSD shapes and can measure accurately α_H , α_L , and v_B . In the optical band we require even more. We need to be able to measure those same three parameters over the frequency range where we expect reprocessed X-rays to be found. However, we need to extend to even lower frequencies to test whether there are any other components in the optical variability, for example the intrinsic disc variations suggested by Arévalo et al. (2009) and Breedt et al. (2010).

The above requirements limit the number of AGNs that can be observed in a human lifetime. In particular, we require a low-mass AGN where time-scales are shorter and more accessible. The best candidate is NGC 4395. Although its exact mass is still under debate, there is agreement that it is very low. From UV line reverberation mapping, generally considered to be one of the better methods for measuring AGN masses, Peterson et al. (2005) derive a mass of 3.6 \times $10^5 \mathrm{M}_{\odot}$ and, from gas dynamical modelling, den Brok et al. (2015) derive $4 \times 10^5 \mathrm{M}_{\odot}$. However, from optical photometric reverberation, aimed mainly at H_{α} , Edri et al. (2012) derive $4 \times 10^4 \mathrm{M}_{\odot}$, Woo et al. (2019) derive $1 \times 10^4 M_{\odot}$, and Cho et al. (2021) derive $1.7 \times 10^4 M_{\odot}$. The exact value is not critical to the analysis presented here as the median point of the g '-band response function, which we use later to synthesize an optical light curve based on an X-ray light curve, is fixed by observations of the X-ray to g'-band lag (McHardy et al. 2023). Thus, if we chose a low mass, we would simply increase the accretion ratio to produce a response function broadly similar to that of a higher mass and lower accretion ratio.

NGC 4395 is also well observed in both X-ray and optical/UV bands. The X-ray PSD is well defined from *XMM–Newton* observations. From a single orbit (\sim 120 ks) observation Vaughan et al. (2005) obtained a good fit with a breaking power law with $\alpha_H = 1.92^{+0.28}_{-0.24}$, $\alpha_L = 1.2^{+0.76}_{-0.4}$, and $\nu_B = 1.9^{+0.8}_{-1.5} \times 10^{-3}$ Hz. Thus, the break, or bend, time-scale is a very accessible \sim 500–1000 s.

We have subsequently observed NGC 4395 for a further four *XMM*–*Newton* orbits, (Vincentelli et al., in preparation and Beard et al., in preparation) which broadly confirm these PSD parameters.In this paper, we use these new X-ray data, together with X-ray data

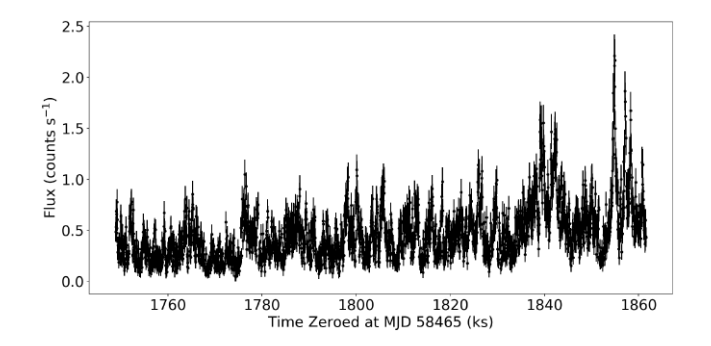


Figure 1. *XMM*–*Newton* 0.5–10 keV light curve for NGC 4395 using data from the night of 2019 January 2, binned up to 50 s.

covering longer time-scales from *Swift*, to simulate optical light curves, assuming disc reprocessing, and hence to produce model optical PSDs. These model PSDs are then compared with the real, observed, optical PSD to determine whether disc reprocessing can account for all of the observed optical variability.

To produce the observed optical PSD the highest frequencies, 4×10^{-4} to $\sim 10^{-1}$ Hz, are provided by recent very high quality simultaneous ugriz monitoring with 3 s-sampling over 6 h using HiPERCAM on the 10.4m Gran Telescopio Canarias (GTC) (McHardy et al. 2023). Intermediate frequencies (approx 5×10^{-7} to 4×10^{-4} Hz) are provided by TESS (Burke et al. 2020). To cover the lowest frequencies, $\sim 2 \times 10^{-8}$ to 2×10^{-6} Hz, we combine these data with nightly g'-band observations over a period of 3 yr with a number of ground-based telescopes, including the Liverpool Robotic Telescope (LT), the Las Cumbres Observatory (LCOGT), the Zwicky Transient Factory (ZTF), and the Zowada Observatory. We also include V-band data with 2 d sampling from two 4 month observation periods with Swift (Cameron et al. 2012). Thus, overall, we are able to determine the optical PSD from $\sim 2 \times 10^{-8}$ to $\sim 10^{-1}$ Hz.

The X-ray and optical observations are presented in Section 2. In Section 3, we derive the synthetic optical light curves expected from disc reprocessing of the new *XMM–Newton* X-ray light curves. In Section 4, we derive both the observed and synthetic optical PSDs and in Section 5, we compare these PSDs and discuss the implications of the comparison.

2 OBSERVATIONS

In this section, we present the observations that will be used later in this paper.

2.1 XMM-Newton observations

Four separate \sim 117 ks X-ray observations from the *XMM–Newton* EPIC PN were taken, beginning on the 2018 December 13, 19, and 31 and 2019 January 2. The data were analysed in the standard manner using the ESA XMM–SAS 19 software. We extracted source plus background events in 10 s time bins in the energy band 0.5–10 keV from a circle of radius 30 arcsec around the AGN, filtering events with PATTERN< = 4 and FLAG= = 0. The background was taken from a nearby blank area of the detector of the same size. As an example the light curve from the fourth observation, binned up to 50s, is plotted in Fig. 1.

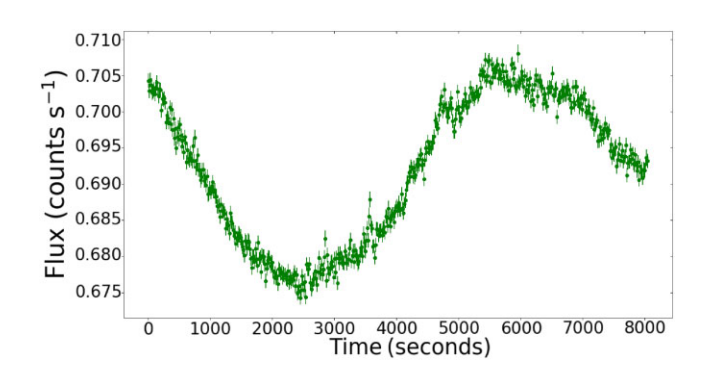


Figure 2. GTC HiPERCAM SDSS *g'*-band light curve zeroed to MJD 58224.87378.

2.2 Optical observations

For a valid comparison of the observed and synthetic optical PSDs, both PSDs must be in the same waveband. Here, we choose the g'-band for a number of reasons. Almost all ground-based telescopes have g'-band filters and detectors are also quite sensitive in the g'-band, thus good quality g'-band light curves can be obtained reasonably easily. Although fractional variability is higher in the g band, telescope sensitivity is considerably less and atmospheric absorption is more of a problem, so it is very hard to obtain long, high-quality, g-band observations. The g' band is a good compromise. For some observatories, particularly g-band is a good compromise. For some observatories, particularly g-band is a good compromise are available. In that case, we adjust the variations in the g-band observations from the g-band. Here, we present new g-band observations from the LT, LCOGT, Zowada, and ZTF and also show previously published optical light curves from g-band g-band g-band g-band optical light curves from g-band g-band g-band g-band g-band optical light curves from g-band g-band g-band g-band optical light curves from g-band g-ban

2.3 Short time-scales: seconds - hours

HiPERCAM: McHardy et al. (2023) carried out very high S/N simultaneous ugriz multiband monitoring of NGC 4395 with HiPER-CAM (Dhillon et al. 2021) on the 10.4 m GTC¹ for 22 ks continuously on the night of 2018 April 16–17. In Fig. 2, we show the first 8000 s of the HiPERCAM g'-band light curve, with 15 s sampling. Tracking problems slightly affected the later parts of the light curve so we do not use them here. As we are using these data to measure very high frequencies, slight loss of lower frequencies, which are covered by TESS (below) is unimportant.

Multiband monitoring, including g'-band, was carried out over five nights with the LT (McHardy et al. 2023) and over two nights on the Faulkes North Telescope (FTN) (Montano et al. 2022). Both the LT and FTN are 2m telescopes. Given also that HiPERCAM has a higher throughput than the instruments on the LT and FTN, and no dead time, the HiPERCAM light curves are of much higher S/N so we do not consider the short time-scale LT and FTN light curves further.

2.4 Medium time-scales: days – month

TESS: A detailed light curve with 15 min sampling for a month from the *TESS* is shown by Burke et al. (2020) and is the basis for their time series analysis. *TESS* observes in a wide, 600–1000 nm bandpass. Variability amplitude and hence power spectral normalization are a function of wavelength. In the standard 'rms/mean' power spectral



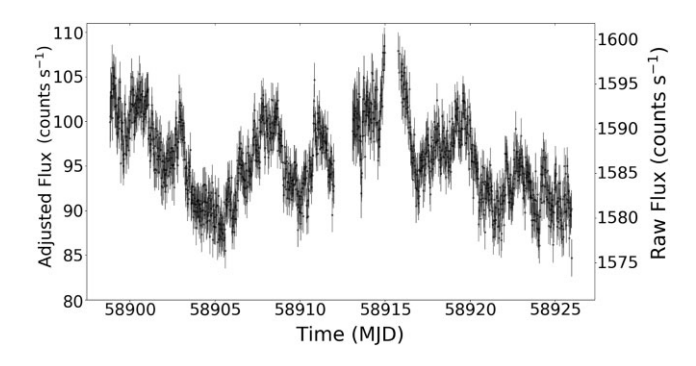


Figure 3. *TESS* light curve for NGC 4395 using data from Burke et al. (2020). The scale on the right-hand *y*-axis gives the original count rate. The scale on the left-hand *y*-axis gives the count rate after subtraction of the constant required to produce a light curve with the same fractional variation as the LT *g'* band over the same time range.

normalization which we use below we should therefore adjust the mean level of the *TESS* light curve by subtracting an appropriate constant so that the resulting power spectral normalization is similar to that expected of a *g* '-band light curve covering the same frequency range.

We could calculate that constant by synthesizing a white light light curve from the appropriately weighted ugriz HiPERCAM light curves and calculating the resultant PSDs. However, there is an additional consideration with TESS in that the pixels are very large and hence there is a large non-AGN constant contribution to the light curve. This constant must also be removed. We can, in fact, correct for both problems by altering the zero level of the TESS light curve so that the resultant fractional variation, $F_{\rm var}$, i.e. standard deviation divided by the mean, of the TESS light curve is the same as that of the long term g'-band light curve discussed in Section 2.5 over a similar length of time as that of the TESS light curve. The resultant light curve can be seen in Fig. 3.

2.5 Long time-scales: months – years

LT, LCOGT, ZTF, Zowada: The main new data presented here are long term SDSS g'-band light curves from the LT's IO:O camera (Steele et al. 2004), the LCOGT McDonald Observatory's Sinistro and Faulkes Telescope North's (FTN) Spectral cameras (Brown et al. 2013), the Zowada Observatory (Carr et al. 2022) and the ZTF (Masci et al. 2018). The details of the observations can be found in Table 1.

The LT and LCOGT data were processed with aperture photometry using the HiPERCAM pipeline, as described in McHardy et al. (2023), using the same comparison star, Star 1, as shown in figs 1 and 12 of McHardy et al. (2023) and with the same source aperture radius of 4.25 arcsec. The ZTF light curve was extracted from the images by the Automated Learning for the Rapid Classification of Events (ALeRCE) pipeline (Masci et al. 2018)² and the light curves were then downloaded from the ALeRCE ZTF Explorer.³ Zowada fluxes were also obtained by differential aperture photometry using in-house code which compares the AGNs with a number of stars in the field (Carr et al. 2022).

The light curves were initially in a variety of different units so to combine them we first converted them all into mJy. The LT and LCOGT light curves were initially in units of counts/sec relative

²https://alerce.science/alerce-pipeline/

³https://alerce.science/services/ztf-explorer/

Table 1. SDSS g'-band observations.

Observation name	Exposure time	Number of obs	Start date	Stop date
LT IO:O	40s (until 2021 August 2)/60 s (after)	342	2019 November 9	2022 July 22
LCOGT	45 s (Spectral)/240 s (Sinistro)	128	2019 December 28	2022 July 11
ZTF	30s	97	2019 November 2	2021 July 2
Zowada	5×300 s	13	2022 February 24	2022 March 28

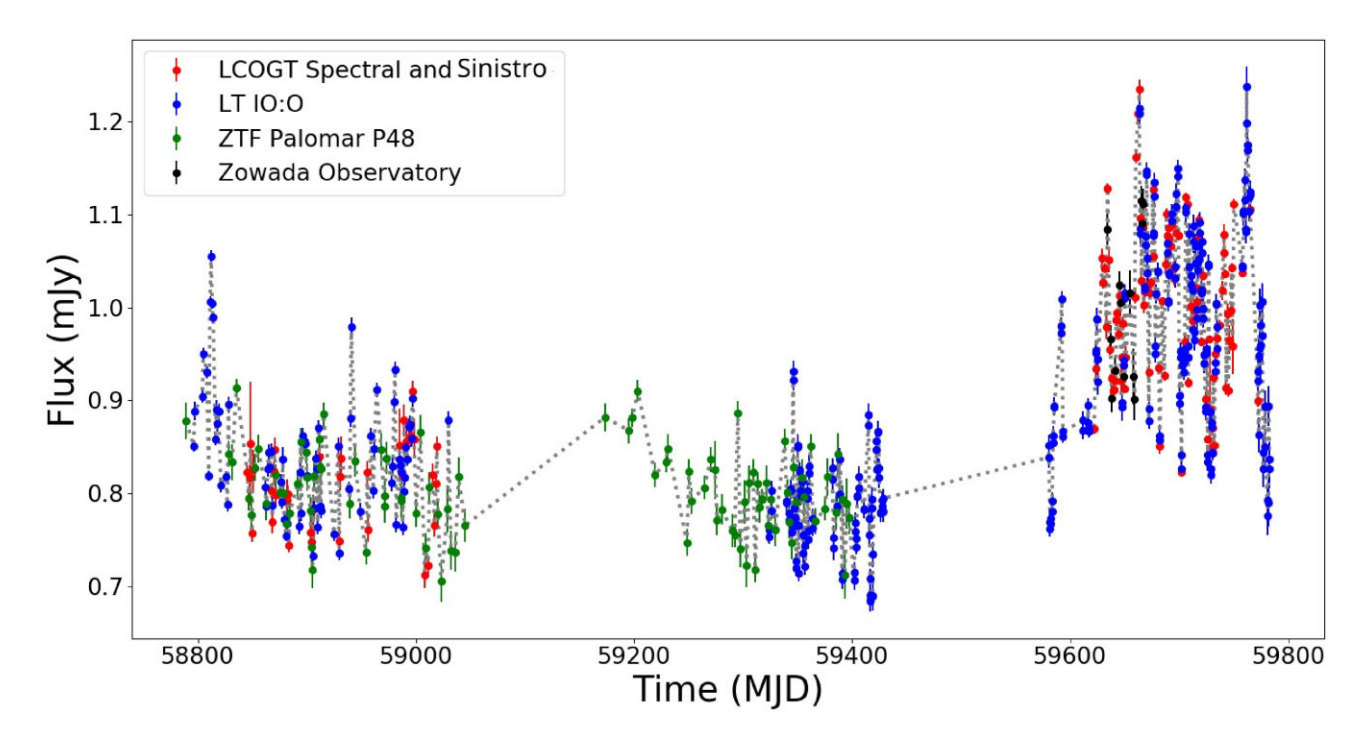


Figure 4. Long term SDSS *g*'-band light curve for NGC 4395 comprised of data from Liverpool Telescope, Las Cumbres Observatory, Zowada Observatory, and the Zwicky Transient Facility.

to comparison Star 1 and magnitudes are available for Star 1 from SDSS which we converted to mJy. The ZTF light curve is in AB magnitudes which we again convert to mJy. The Zowada data were provided directly in mJy.

To ensure good cross-calibration between the various light curves, points with common time stamps were compared and then a Chi-squared minimization of an additive and multiplicative translation was applied (relative to the LT data). This procedure created the light curve seen in Fig. 4. Due to seasonal breaks, the light curves are divided into three 'epochs' by which we will refer to them.

Swift: There was long time-scale optical monitoring by Swift in 2008–2009 (Cameron et al. 2012) over two periods of duration 112 and 161 d, separated by a 76 d gap, with typical 2 d sampling. In Fig. 5, we present again the Swift Ultraviolet and Optical Telescope (UVOT) B and V band light curves from the longer, second, period. The first period contains an outburst of amplitude larger than that seen in other observations of this source. The concern then is that the assumption made by most authors who analyse AGN temporal variability, including ourselves, i.e. that the variability is a statistically stationary process, might not be valid. However, in Section 4, we show that the PSD of the first period is consistent with the PSD of the second period and so the outburst is probably just part of the normal variability of the source. Thus, although we note the caveat, we proceed on the assumption that the variability is

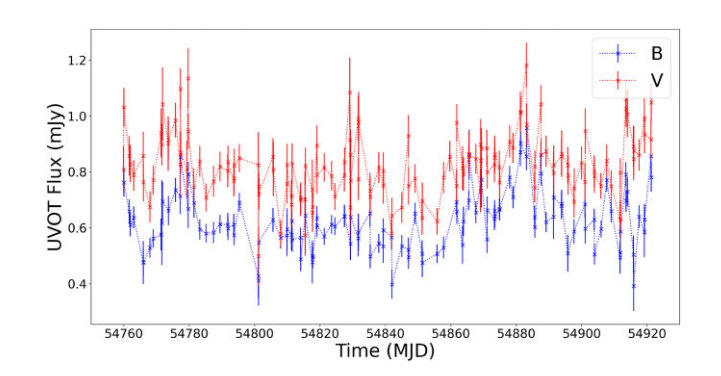


Figure 5. Swift UVOT light curve for NGC 4395 from Cameron et al. (2012).

statistically stationary and so normal PSD analysis methods may be used. The first period is, however, short and adds very little to our long time-scale temporal coverage so we do not in fact consider it elsewhere.

3 SIMULATING LONG-TERM OPTICAL LIGHT CURVES

We simulate long time-scale optical light curves by reprocessing long time-scale X-ray light curves by an accretion disc model. The longest observed high quality X-ray light curves, from XMM-Newton, are only of maximum duration \sim 140 ks. Therefore, we first have to simulate much longer X-ray light curves, of similar quality, but which include the long term variability properties.

3.1 Simulating long-term X-ray light curves

3.1.1 Quantifying X-ray variability

The main variability characteristics of a light curve are usually quantified in terms of its PSD. AGN X-ray PSDs are often well described by bending power laws (M^cHardy et al. 2004) given by

$$P(v) = Av^{-\alpha_L} \left(1 + \left(\frac{v}{v_B} \right)^{\alpha_H - \alpha_L} \right)^{-1} + C, \tag{1}$$

where v_B is the bend frequency, α_H and α_L are the high-frequency and low-frequency slopes, respectively, and A and C are constants. As noted in M^cHardy et al. (2004), an arbitrarily large number of bends can be incorporated by daisy-chaining the above equation. A double-bending power law, which will be used later in this paper, is therefore given by

$$P(\nu) = A\nu^{-\alpha_L}\gamma^{-1} + C \tag{2}$$

with

$$\gamma = \left[\left(1 + \left(\frac{\nu}{\nu_{B1}} \right)^{\alpha_M - \alpha_L} \right) \left(1 + \left(\frac{\nu}{\nu_{B2}} \right)^{\alpha_H - \alpha_M} \right) \right].$$

If the PSD parameters are known, light curves similar to the observed light curves can be simulated using the method of Timmer & König (1995). However, this method produces only Gaussianly distributed light curves and the X-ray light curves NGC 4395 are not Gaussianly distributed (i.e. to first approximation, they are not evenly distributed about the mean and are more 'burst-like'). We therefore use the method of Emmanoulopoulos et al. (2013) where the parameters of the flux probability density function (PDF), as well as the PSD parameters, are included.

These PSD and PDF parameters are derived directly from observations, here using our recent long XMM–Newton light curves, using PYTHON code⁴ written by Connolly (2015). However, these X-ray observations do not cover the longer time-scales (~years) that we require for comparison with our observed long time-scale g'-band light curve. In particular the slope of the X-ray PSD on long time-scales, α_L , is not well determined. However, we can estimate α_L by using the earlier Swift observations (Cameron et al. 2012).

3.1.2 Measuring the low-frequency X-ray PSD slope

The four new observed *XMM–Newton* observations are well fitted (fit probability, P=0.79) by a bending power-law model with $\alpha_L=0.8^{+0.2}_{-0.3},~\alpha_H=2.3^{+0.1}_{-0.2},~\text{and}~\nu_B=7.7^{+10.2}_{-6.5}\times10^{-4}~\text{Hz}.$ These values are similar to those of Vaughan et al. (2005) for the same bending power-law model. In particular, Vaughan et al. (2005) give $\alpha_L=1.20^{+0.40}_{-0.76}$ so their value and ours are similar to that of all other AGNs where that slope is reasonably well measured.

Although the sampling of the *Swift* data (2 d) is much lower than that of the *XMM*–*Newton* data, we can derive a combined *Swift* and *XMM*–*Newton* PSD, which extends our measurement of α_L to years

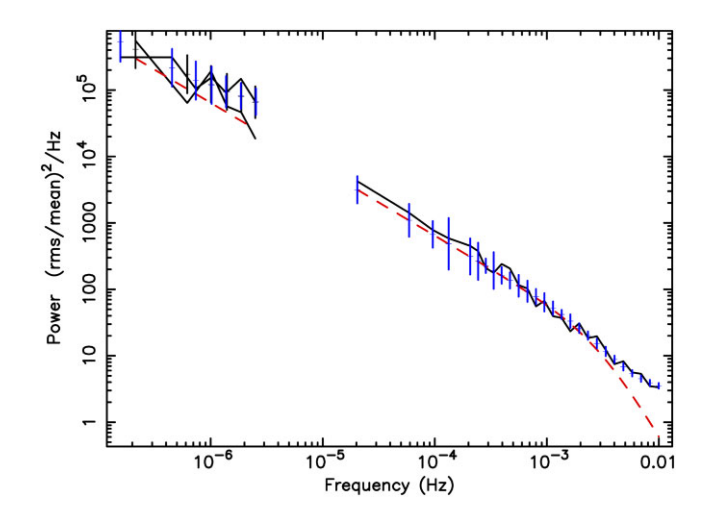


Figure 6. Combined *Swift* and XMM PSD. The data are represented by the continuous solid lines. The dirty model is represented by the errorbars and the underlying PSD is given by the dashed line.

time-scales using PSRESP. PSRESP properly takes account of red noise leak, aliasing, and window effects in the PSD caused by the sampling pattern to reveal the true underlying PSD shape. We refer readers to Uttley et al. (2002), and to other papers which have used PSRESP (e.g. McHardy et al. 2004), for details of the method. The resulting PSD is shown in Fig. 6 and is well described by a bending power-law model.

The average flux in the first part of the Swift light curve is about four times higher than in the second part. However, the pattern of variability as quantified by the power spectrum in standard units of (rms/mean)²/Hz, where the mean is the local mean of the particular part, is very similar and so we include both parts here separately. The resulting 90 per cent confidence limits on the low-frequency slope are 0.75 and 1.1 which is consistent with a fit where the low-frequency slope determined just from the XMM-Newton fit extrapolates reasonably well to lower frequencies. Thus, for the present, we use the PSD and PDF parameters determined from fits to the XMM-Newton data, assuming that α_L does extrapolate smoothly to years time-scales, to simulate long-time-scale X-ray light curves. Better sampled Swift observations are currently under way to improve our determination of the low-frequency X-ray PSD. When complete they will be the subject of future work but they are beyond the scope of this paper.

3.1.3 Comparison of observed and simulated X-ray PSDs

Using the PSD and PDF parameters determined from those observations, and assuming that the low-frequency PSD is an extension of that measured with *XMM–Newton*, we can now simulate X-ray light curves which are arbitrarily long and arbitrarily well sampled.

The main feature in the X-ray PSD is a bend at a time-scale of \sim 1300 s. To simulate accurately this feature, including the PSD slopes both below and above this time-scale, we retain the same 10 s sampling as the original observed *XMM–Newton* light curves. Although it is then quite computationally expensive, we simulate X-ray light curves of duration 10 d which, following convolution with the g'-band disc response function (Section 3.2), will produce

⁴https://github.com/samconnolly/DELightcurveSimulation

⁵https://github.com/wegenmat-privat/psresp

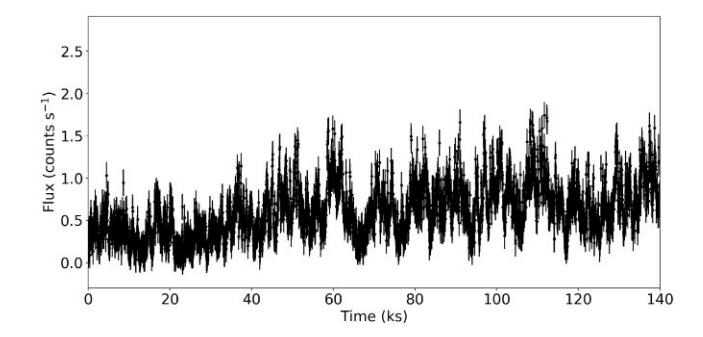


Figure 7. A 140 ks sample of the simulated X-ray light curve using data from the night of 2019 January 2, binned up to 50 s for visual clarity.

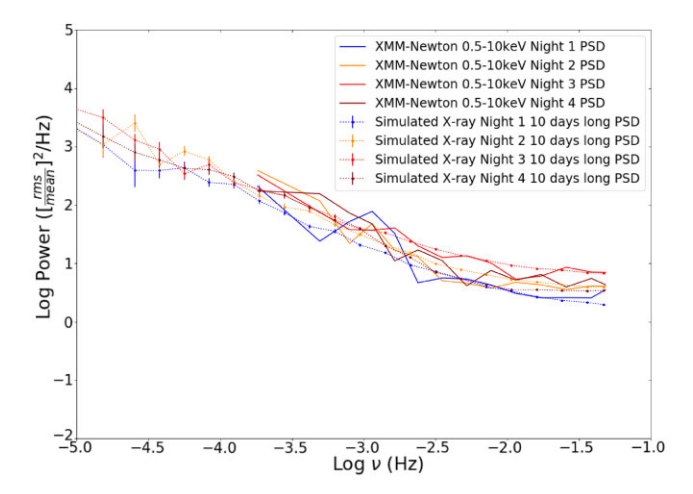


Figure 8. The 0.5–10 keV X-ray power spectra from the *XMM–Newton* data plotted with the PSDs of those same nights' simulated X-ray power spectra.

optical light curves which contain many samples of all likely time-scales of disc variability. An example of a simulated *XMM–Newton* X-ray light curve of similar length (140 ks) to the observed light curves is shown in Fig. 7.

We simulate light curves based on each of the four separate *XMM—Newton* observations to check for variation. To check that our analysis is self-consistent we show, in Fig. 8, the observed PSDs from our four *XMM—Newton* observations and also the PSDs derived from 140 ks sections of each of the simulated light curves. The observed PSDs all overlap and the simulated PSDs lie within the range covered by the scatter in the observed PSDs so, although not all identical, they are consistent with being part of the same variability process.

3.2 Model optical light curves from X-ray simulations

As the PSDs from all four *XMM*—*Newton* observations are very similar then, to avoid unnecessary computation, we choose, somewhat arbitrarily, just one long X-ray light curve, simulated from the 2019 January 2 observation. We convolve this light curve with a model disc response function from KYNREVERB (Kammoun et al. 2021). As our observed optical data is either g'-band or calibrated to be g'-band, we use a g'-band response function using the same input parameters as found in Beard et al. (in preparation), i.e. zero spin, $10 \, R_g$ corona height, a colour correction factor, $f_{\rm col}$, of 1.5, and a disc outer radius of $1500 \, R_g$. These numbers are very similar to those derived by McHardy et al. (2023) from modelling the inter-band lags

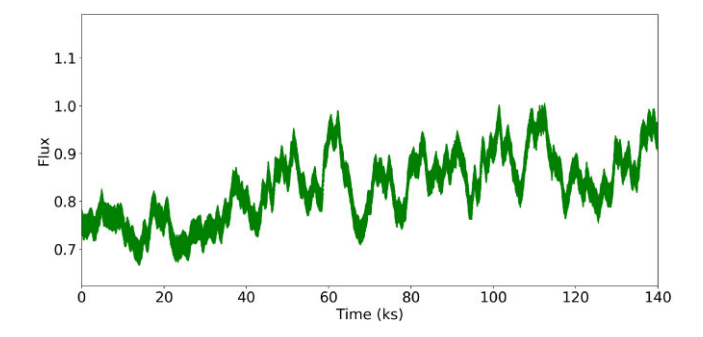


Figure 9. A 140 ks sample of the synthetic g'-band light curve created from the simulated X-ray LC in Fig. 7, binned up to 50 s for visual clarity.

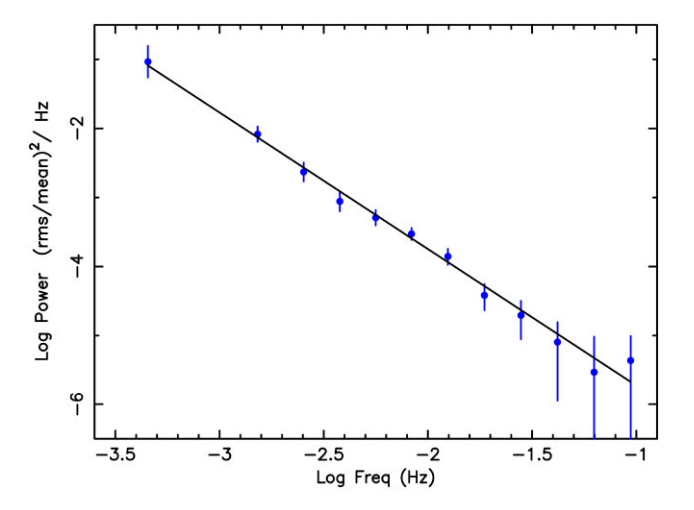


Figure 10. PSD of *g'*-band HiPERCAM observation with Poisson noise removed.

but are slightly modified to fit the new *XMM–Newton* X-ray and UV lag data.

The g'-band lags the X-rays by about 800 s (McHardy et al. 2016, 2023). The observed lag corresponds to the median of the g'-band response function. Kammoun et al. (2021) show that the response from a disc drops, from the peak, to time-scales $50 \times$ longer than the median lag (see their fig. 8), by a factor $\sim 10^4$ which, for NGC4395, is ~ 0.5 d. Thus, our 10 d long simulated light curves contain many samples of even this extremely low part of the response function and so are a good representation of what we might expect from reprocessing central X-rays by a surrounding accretion disc.

For comparison with the simulated one-orbit XMM–Newton 140 ks X-ray light curve (Fig. 7), a 140 ks sample of the synthetic g'-band light curve is shown in Fig. 9.

4 COMPARISON OF OBSERVED AND SIMULATED OPTICAL PSDS

4.1 Observed optical power spectrum

4.1.1 The HiPERCAM PSD

We begin by showing (Fig. 10) the PSD of the HiPERCAM g'-band data alone at the original 3 s-sampling, produced using the standard method of Deeming (1975) for discretely sampled data. This PSD is well fitted (P=0.91) by a combination of a power law of slope 2.00 ± 0.18 together with Poisson noise. Here, the Poisson noise

power has been removed. Aliasing does not affect these data but there may be a little red noise leak at the lowest frequencies. No complex modelling has been carried out. For an underlying slope of 2, red noise leak does not change that slope, but it does increase the normalization, which we will deal with below. The measured slope is in very good agreement with the value expected from a DRW (2.0), or the value of the high-frequency slope of the broken power law (1.88 \pm 0.15) fitted to the PSD of the TESS data (Burke et al. 2021), which covers the two decades of frequency immediately below the HiPERCAM range. Thus, the initial indications are that a single unbending power law covers most of the frequencies sampled by TESS and HiPERCAM.

4.1.2 PSRESP modelling of the full data set

To measure the full optical PSD covering time-scales from years to ~ 10 s, we combine the HiPERCAM and TESS data with other observations described in Section 2 covering longer time-scales. To properly take account of PSD distortions caused by sampling irregularities, red noise leak, aliasing, and Poisson noise from counting statistics which flatten the observed PSD at high frequencies, we model these data using PSRESP (Uttley et al. 2002), following the prescription described by Uttley et al. and used in previous papers (e.g. McHardy et al. 2004). In PSRESP the 'dirty' PSD, derived from the raw observations and therefore distorted by the window function of those observations and including the contribution from Poisson noise, is first calculated. From an assumed underlying undistorted model PSD, light curves are simulated and sampled with the same window function as the observed data. The resulting simulated dirty PSD is then compared with the observed dirty PSD. The parameters of the underlying undistorted PSD are then varied to obtain the best match between the observed and simulated dirty PSDs. Following multiple simulations, uncertainties can then be derived on the simulated dirty model PSD, rather than on the observed dirty PSD. See Uttley et al. (2002) for more details.

To cover the highest frequencies, we include the HiPERCAM g'band light curve of duration 8000 s. As PSRESP is computationally intensive we bin these data to 15 s. For intermediate frequencies we input the TESS light curve, renormalized to g'-band variability, of duration 28 d, in \sim 2 ks bins. At the lowest frequencies, we have the LT, LCOGT, Zowada, and ZTF g'-band light curves which cover 3 yr, but with seasonal gaps. We input the three seasonal sections as epochs 1, 2, and 3, binned at \sim 1.75 d, which is the average sampling period. We also input separately the Swift B and V light curves from the second, longer, section. This section is of similar length to epochs 1, 2, and 3 so the binning is the same. Spectrally, the B and V bands are close to g' band, on either side, so variability amplitudes should not be very different, with B expected to be slightly more variable and V less variable. As the number of data points is not large we do not renormalize them, with the post-facto justification that their resultant PSDs are almost identical.

For the very lowest frequencies longest time-scales we input the entire 3 yr light curve in one piece. We bin it into 80 d bins to cover the seasonal gaps and, with that large binning, we do not duplicate the frequency coverage obtained from the smaller binning of each individual epoch. For the PSRESP simulation of this light curve, we set the sampling to a shorter time-scale (0.3 d) so that the high-frequency variations are included, and then bin up to 80 d. This then gives us some useful extra long-term power in the $\log(\nu/\text{Hz})$ range -7 to -8.

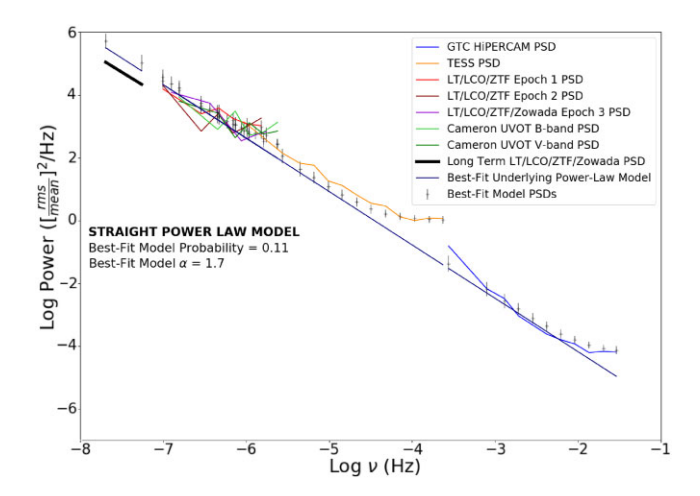


Figure 11. The observed 'dirty' optical power spectra are shown by continuous, zigzag, lines with different colours indicating the different source light curves as indicated in the legend. The corresponding best-fit model PSDs, assuming an underlying unbending power-law PSD, are shown by the error bars. The underlying power law is shown by the smooth, continuous, straight line

Unbending power-law fit: We first use PSRESP to determine whether a simple unbending power law provides an adequate description of the data. The best-fit to such a model is shown in Fig. 11. The best-fit slope is $1.7^{+0.6}_{-1.0}$ with P=0.11. Whilst not bad enough to entirely rule out this model, the fit probability is low and, visually, there appears to be a flattening at the lowest frequencies.

Low resolution bending power-law fit: We next fit the PSD with a bending power law. Although, the fit to an unbending power law had indicated that the deviation from a single power law occurred towards the lower end of the frequency range which our data samples, we none the less began with a search for a bend over the full frequency range sampled from 10^{-8} to 10^{-1} Hz. Performing a fit with high resolution in frequency over such a wide frequency range is computationally very time consuming so, to narrow down the parameter range to search over, we began with a search at low resolution. We searched initially with resolution of a factor 2, i.e. 0.3 in log(v), between searched frequencies. We sampled the high-frequency slope between 1.5 and 2.5 in steps of 0.5 and the low-frequency slope between 0 and 2.0 also in steps of 0.5. This search generated a best-fit of P = 0.57 with $\log(v_B) = -5.6^{+2.4}_{-0.6}$ (i.e. $v_B = 2.5^{+640}_{-1.9} \times 10^{-6}$ Hz), $\alpha_H = 2.0^{+0.5}_{-0.0}$, and $\alpha_L = 1.0 \pm 0.5$. The large upper error on ν_B is a consequence of the large step sizes and poor resolution and the zero error on the lower limit to α_H is a result of hitting the end stops of the search range.

High resolution fit with fixed α_H : As the best-fit to α_H from both the HiPERCAM and TESS data individually is 2.0, and as the best-fitting value from our initial rough fit is also 2.0, we next fixed α_H at 2.0 and performed a search with higher resolution in ν_B (factor 1.5) and α_L (steps of 0.1). A contour plot of the fit probabilities for these two parameters is shown in Fig. 12. This plot shows that α_L is very close to 1 and that ν_B lies in the range 10^{-7} to 10^{-5} Hz.

High resolution fit with all parameters free: We finally performed a high resolution fit over all three parameters, restricting ν_B to the range 10^{-7} to 10^{-5} Hz, with factor 1.5 steps in frequency. The search range for α_H is 1 to 4, in steps of 0.1 and the range for α_L is 0 to 2, also in steps of 0.1. The resultant best-fit is plotted in Fig. 13. The fit is very good, with a best-fit model probability of P=0.66 with $\alpha_H=2.1^{+0.2}_{-0.4}$,

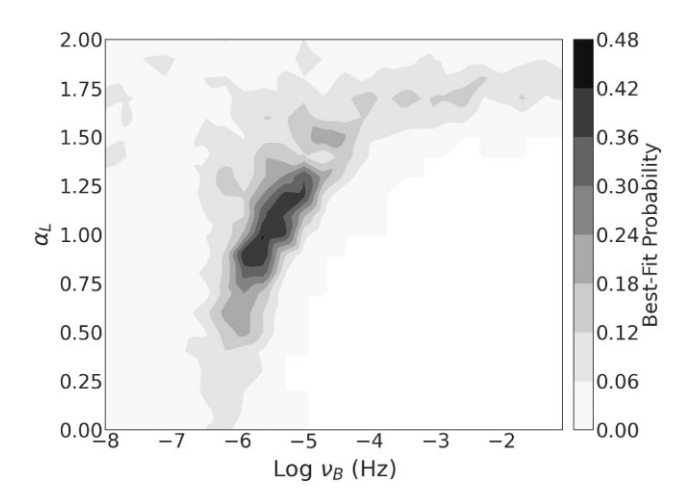


Figure 12. Best-fit probability contours of v_B versus α_L with α_H fixed at 2.0

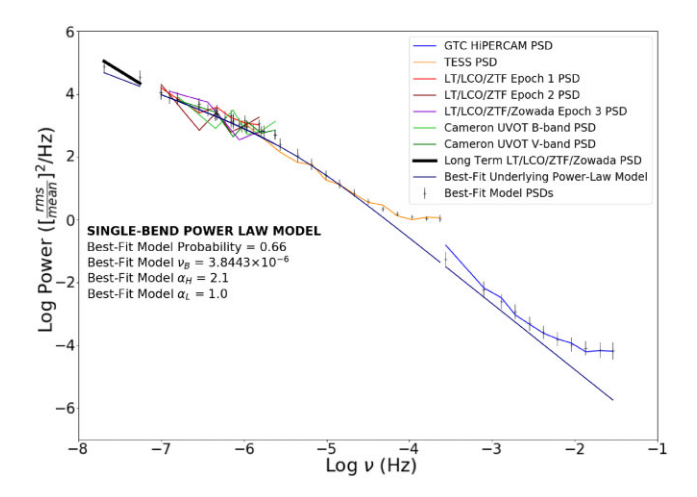


Figure 13. The observed 'dirty' optical power spectra are shown by continuous, zigzag, lines with different colours indicating the different source light curves as indicated in the legend. The corresponding best-fit model PSDs, assuming an underlying single-bend power-law PSD, are shown by the error bars. The underlying power law is shown by the smooth, continuous line with a single bend.

 $\alpha_L=1.0^{+0.2}_{-0.2},$ and $\nu_B=3.8^{+4.8}_{-2.6}\times10^{-6}$ Hz, corresponding to a bend time-scale of $3.05^{+6.6}_{-1.7}$ d.

Taking the bend time-scale as $1/\nu_B$, we obtain a value of 3 d, which is very similar to the 2.3 d DRW damping time-scale measured by Burke et al. (2020). Burke et al. (2020) also fit what they refer to as a broken power law which, functionally, is the same as the bending power law used here. They list the break frequency as 0.114 ± 0.066 d⁻¹ which, taking the simple reciprocal as a measurement of the time-scale, for comparison with our measurement, gives a bend time-scale of 8.8 d. However Burke et al. (2020) do not make strong claims for the precision of their bend time-scale as the bend is very close to the lower limit of the frequencies covered by the *TESS* data, which are better covered here.

The high-frequency slope measured here is in very good agreement with that (1.88 \pm 0.15) measured by Burke et al. (2020) from their broken power law. The main difference between the present analysis and that of Burke et al. (2020) is that we find a low-frequency PSD slope of 1.0 \pm 0.2 rather than the 0.00 \pm 0.86 of the broken power law or the 0 required by the DRW model. However, again we note that

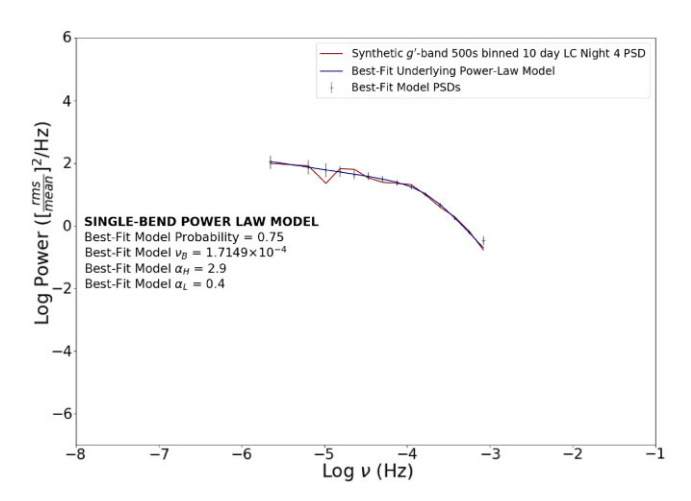


Figure 14. The synthetic g'-band PSD from the synthetic 10 d light curve based on the *XMM–Newton* night 4 data. Also plotted are the best-fit model PSD as well as the best-fit underlying power law for a bending power law model. This plot uses the same axes limits as the full observed optical data PSD for ease of comparison.

the *TESS* data provide very little PSD frequency coverage below the bend, whereas here we have nearly two decades. Thus, the uncertainty in the low-frequency PSD slope of Burke et al. (2020) is sufficiently large to allow compatibility with the present results.

A high-frequency slope of 2 is a fixed parameter of a DRW model but just because a DRW model can be fitted to a light curve, it does not mean that the high-frequency PSD slope is exactly 2. The most that we can say is that a measured slope of 2 is consistent with a DRW model.

As we now have a good fit to the observed optical PSD we proceed, in Section 4.2, to determine whether the model PSD derived from X-ray disc reprocessing is consistent with the observed PSD.

4.2 Synthetic optical power spectra

In Fig. 14, we present the PSD resulting from the synthetic optical 10 d g'-band light curve, a section of which is shown in Fig. 9, together with the best-fitting model which has $\nu_B = 1.72^{+0.36}_{-0.75} \times 10^{-4} \, \mathrm{Hz}$ (i.e. a time-scale of 1.6 h), $\alpha_H = 2.9^{+0.1}_{-0.3}$, and $\alpha_L = 0.4^{+0.1}_{-0.3}$. This PSD shows a clear bend at $\sim 10^{-4} \, \mathrm{Hz}$ with a steep high-frequency slope and fairly flat low-frequency slope. This PSD looks similar to the X-ray PSD from which it was generated except that the bend is a decade lower in frequency. The high-frequency slope is also slightly steeper consistent with the expectations from the disc reprocessing. The very pronounced flattening at $\sim 10^{-4} \, \mathrm{Hz}$ in the synthetic PSD is not obviously visible in the observed optical PSD.

The optical light curves from which this PSD were derived were simulated from the X-ray light curves assuming a reprocessing function based on a mass of $3.6 \times 10^5 M_{\odot}$ and a low accretion rate. However, if the mass is actually a decade lower, it will make little difference to the optical light curves and hence to synthetic PSD as the disc reprocessing function is mainly defined by the lags between wavebands, which are fixed. Thus, parameters such as the accretion rate and possibly the colour correction factor (see McHardy et al. 2023) would have to be adjusted to give the same lags.

One possibility is that this bend does exist in the observed PSD but that, in addition to disc reprocessing, there are other causes of variability which produce longer term variations, leading to the bend we detect at $\sim 10^{-6}$ Hz and obscuring the bend at $\sim 10^{-4}$ Hz. In the

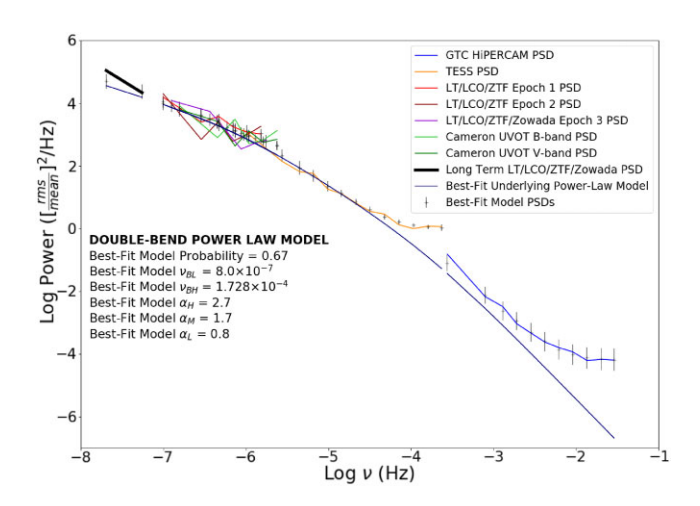


Figure 15. The optical power spectra from our data plotted with their best-fit model PSDs as well as the best-fit underlying power law for a double-bending power law model.

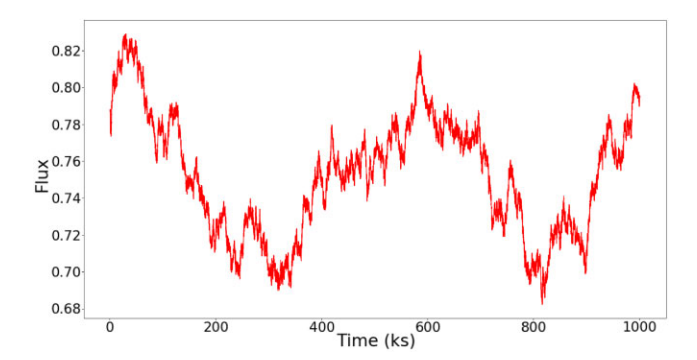


Figure 16. Simulated 10 d light curve using the Timmer & König (1995) method with an input bending power law with bend frequency 10^{-6} , high-frequency slope -2, and low-frequency slope -1.

next section, we explore whether both bends could be present in our data.

4.3 Testing for double-bend compatibility

In Fig. 15, we show the best fit for a PSD with two bends. All parameters were allowed to vary. The low-frequency bend is at $v_{BL} = 8.0^{+2.4}_{-4.3} \times 10^{-7}$ Hz and the high at $v_{BH} = 1.7^{+0.4}_{-0.6} \times 10^{-4}$. The slope below the lowest bend, $\alpha_L = 0.8^{+0.3}_{-0.3}$, the slope between the two bends, $\alpha_M = 1.7^{+0.3}_{-0.2}$, and the slope above the highest bend, $\alpha_H = 2.7^{+0.3}_{-0.5}$. The fit probability (P = 0.67) is almost identical to the fit probability for a single bending power law so it is not, statistically, a better fit. It is, however, still a good fit and the inclusion of a second bend at a frequency near to that expected from reprocessing is consistent with the data. Thus, a combination of reprocessing to explain the high-frequency optical variability and some other variability process, for example intrinsic disc fluctuations, could explain the total observed optical variability.

4.4 The origin of the low-frequency optical variations

To confirm that a combination of reprocessing and a second independent source of variations can explain the observed variability, and to roughly estimate the relative contributions of these two processes, we attempt to reproduce the observed PSD with two such light curves.

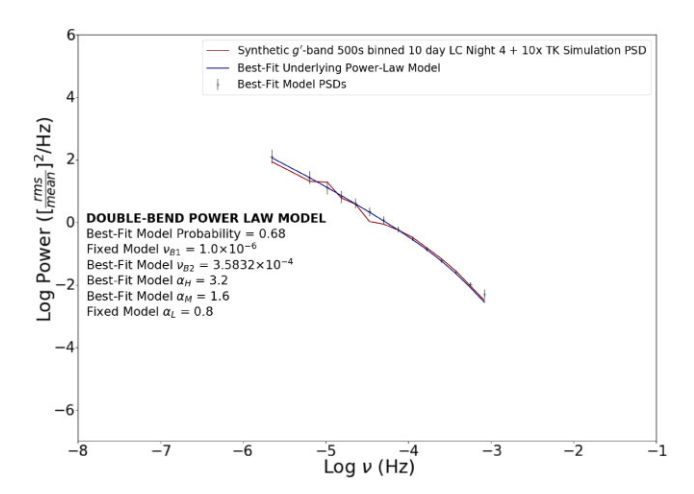


Figure 17. The power spectra from our synthetic g'-band light curve plus $10 \times$ the Timmer & König (1995) simulated light curve plotted with its best-fit model PSD as well as the best-fit underlying power law for a double-bending power law model. This plot uses the same axis limits as the optical data PSD for ease of comparison.

For the reprocessed light curve we use the 10 d one discussed in Section 3.2. As there is no obvious sign in any of the observed optical light curves of the non-linear variations seen in the X-rays, we can simulate the independent source of variations extending to low frequencies using the method of Timmer & König (1995). We take $\alpha_L = 1$, $\nu_B = 1 \times 10^{-6}$ Hz, and $\alpha_H = 2$, seen in Fig. 16.

In the standard PSD normalization of (rms/mean)²/Hz which we use here, the power level of the PSD can be adjusted by changing either the rms or the mean of the input light curve, or both. Here, for the independent source of variations, we take the same mean level as for the reprocessed light curve and alter the rms until we obtain a combined PSD (Fig. 17) which is similar to the observed one. We find that an rms of approximately 70 per cent of the mean, when combined with the reprocessed light curve, is required. This adjusted rms is about 10 times the rms of the reprocessed light curve. However, the exact value should not be regarded as being particularly precise as there are a number of uncertainties involved, for example the exact shape of the reprocessing function which depends on unknowns such as the colour correction factor.

Although, for the computational reasons stated earlier, this PSD does not extend to quite as low frequencies as our observed PSD it does extend far enough for us to determine whether the two combined light curves might provide an explanation of the observed PSD, which it does. We do not claim that this combination is the only possible explanation, just that it is one possible explanation.

4.5 Comparison with previously published optical PSDs

The optical PSD which we have derived here is of very high quality and is well described by a bending power law with $\alpha_L = 1$, $\alpha_H = 2$, and a bend time-scale of 3 d. We briefly compare this PSD with the previously published good quality optical PSDs noted in Section 1 to see whether a similar model, and hence a similar underlying physical mechanism, might apply to them all.

Considering first the bend time-scales, with our extended low-frequency data, we confirm the time-scale measured in NGC 4395 from *TESS* data alone using DRW modelling by Burke et al. (2020). From the present data, we find no requirement for any further bends at lower, or higher, frequencies. Although choice of black hole mass

can alter the slope of the relationship a little, NGC 4395 fits into the relationship between AGN mass and bend (or damping) time-scale which has already been thoroughly discussed by Burke et al. (2021) and so is not unusual as far as bend time-scales go.

The high-frequency slope in NGC 4395 is towards the shallow end of the distribution of *Kepler* high-frequency slopes (Mushotzky et al. 2011; Smith et al. 2018), but is within their distribution. The slope which we simulate based on X-ray reprocessing, 2.9, is towards the steeper end of the *Kepler* slope distributions but is, again, within the distribution. Thus, reprocessing of X-rays is consistent with producing at least some of the high-frequency optical variability but is not necessarily the main contributor.

Low-frequency optical PSD slopes are rarely measured because PSD bends tend to be near the lower end of the range of time-scales sampled. NGC 4395 is a rare exception. The only large sample we are aware of where low-frequency slopes are listed is that of Simm et al. (2016). The sampling of their Pan-STARRS light curves (Simm et al. 2015), typically 70–80 observations over 4 yr though not very evenly spread, required use of CARMA models, rather than Fourier techniques, to estimate PSD parameters. They find an average $\alpha_L \sim 1$. Smith et al. (2018) show bending PSDs for six AGNs but do not list low-frequency slope values. However, four of the six AGNs where bending power laws are required appear to have slopes which are rising towards the lowest frequencies (their fig. 10), although two are falling. Thus the limited previous data are consistent with the better measured α_L presented here.

The one AGN which does not easily fit the pattern discussed above, or is at least an outlier to the distributions, is Zw 229–15, which is probably the best-observed *Kepler* AGN. In the analyses of both Edelson et al. (2014) and Smith et al. (2018) its PSD shows a clear bend. Smith et al. (2018) list a power law slope of 3.4, although it is not clear whether this is a fit to an unbending power law or to the high-frequency part of a bending power law. However Edelson et al. (2014) clearly list $\alpha_H \sim 4$. This slope is at the extreme limits of all listed high-frequency AGN optical PSD slopes. At low frequencies Edelson et al. (2014) list $\alpha_L \sim 2$, steeper than any previous low-frequency slopes. From fig. 10 of Smith et al. (2018), their low-frequency slope appears somewhat flatter but they do not give a slope value.

A possible explanation of the extreme slopes in Zw 229–15 might be if its mass is actually much higher than the $\sim 10^7 M_{\odot}$ noted by Mushotzky et al. (2011) and so the PSD bend detected by Edelson et al. (2014) and Smith et al. (2018) is actually the equivalent of a second, higher frequency bend which, in lower mass AGNs like NGC 4395, would be at too high a frequency to be detected. The low-frequency slope observed in Zw 229–15 and the high-frequency slope in NGC 4395, both having the same slope value of 2, would then just be intermediate slopes in a twice bending power law model. However with the present mass ($\sim 10^7 M_{\odot}$), and with the presently observed bend time-scale, Zw 229–15 fits in well to the mass–time-scale relationship of Burke et al. (2021). There is also no sign of a second high-frequency bend in NGC 4395, even to four decades above the present bend. Thus it is not easy to argue for the second bend hypothesis.

Measurement of PSD parameters is quite dependent on the exact model being fitted and the production of reliable long-time-scale light curves from *Kepler* data is not trivial (e.g. see Edelson et al. 2014; Smith et al. 2018) so some caution in comparisons is required. However on the face of it, the PSD slope values of Zw229-15 may be within the distributions of other AGNs, but they are on the limits of those distributions.

5 CONCLUSIONS

We present new \sim daily optical monitoring of the low mass AGN NGC 4395 over a 3-yr period with the LT, LCOGT, Zowada, and ZTF. Together with 3 s-resolution over a 3 h period by HiPERCAM (McHardy et al. 2023) and monitoring covering time-scales from hours to weeks by *TESS* (Burke et al. 2020), we are able to measure the optical g'-band PSD over an unprecedented range of almost seven decades. The observed optical PSD is well fitted by a bending PSD model with bend frequency of $3.8^{+4.8}_{-2.6} \times 10^{-6}$ Hz, high-frequency slope of $2.1^{+0.2}_{-0.4}$, and low-frequency slope of $1^{+0.2}_{-0.2}$. These parameters, particularly the low-frequency slope, are probably the most accurate yet measured for an AGN optical PSD, but are broadly within the distribution of these parameters as measured from less extensive data by previous researchers.

To test whether the observed PSD can be reproduced by reprocessing of X-rays by an accretion disc we have simulated g'-band light curves based on reprocessing of X-ray observations, similar to those observed by XMM-Newton and Swift, from a disc. The g'-band disc response function used is similar to that required to explain the inter-band lags in NGC 4395 (McHardy et al. 2023), slightly modified to take account of new XMM-Newton data (Beard et. al, in preparation). The PSD of the resulting reprocessed light curve is also well fitted by a bending power law but with a bend frequency almost two decades higher in frequency than that in the observed PSD. The longer bend time-scale in the observed PSD is, however, close to the DRW damping time-scale found from analysis of just the TESS data (Burke et al. 2020), although that time-scale is towards the bottom of the range of time-scales covered by TESS. The PSD slope below the bend, $\alpha_L = 1.0$, which we are able to constrain well with the 3 yr time-scale light curve presented here is, however, steeper than the equivalent PSD slope expected from a DRW, i.e. $\alpha_L = 0$. Our observations are therefore inconsistent with the DRW model for AGN optical variability.

To test whether a second PSD bend, at the higher frequency implied from disc reprocessing, is compatible with the observed PSD we fitted a model with two bends. The resultant fit does recover both lowand high-frequency bends at frequencies similar to those mentioned above, but the fit probability is no improvement on the single bend model. We are able to simulate the observed double-bending power law PSD by the addition of a separate light curve, generated using the formalism of Timmer & König (1995), to the synthetic light curve generated from X-ray disc reprocessing. This second light curve dominates the low-frequency variability.

The origin of this second, dominant, source of variability is, at present, unknown. Reprocessing by the Broad-Line Region (BLR), or some mixture of disc wind and BLR (Elvis 2000; Hagen et al. 2024) which is larger than the disc, will be on longer time-scales than disc reprocessing and so may be candidates. The long tails to the reprocessing functions derived by MEMECHO mapping (Horne et al. 2004) of NGC 4593 (M°Hardy et al. 2018) are factors of a few longer than the duration of the disc response function and may represent reprocessing in the BLR. In many AGNs, e.g. NGC4593 (Cackett et al. 2018), a clear signature of reprocessing in the BLR is detected as a longer lag in the *u*-band, approximately a factor of 2 or 3 longer than the expected disc lag. Frequency-resolved lag analysis of several AGNs also shows that the observed lags on time-scales of tens of days are longer than can be explained by a standard disc reprocessing model (Cackett, Zoghbi & Ulrich 2022; Lewin et al. 2023).

Thus although the BLR may well contribute power to the PSD on longer time-scales than the disc, it is unclear whether the BLR can provide power on time scales $100 \times$ longer than the disc, as required by our observations. This possibility requires further investigation.

An alternative possibility which might more easily explain the long-time-scale variations, as it is related to viscous rather than light travel time-scales, is inwardly propagating disc accretion rate variations (Arevalo & Uttley 2006). The slow-moving radial disc temperature variations recently found in AGN discs (Neustadt & Kochanek 2022) may be related to this phenomenon, although no claim has yet been made for the origin of these temperature variations.

We conclude that reprocessing of central X-rays by a surrounding accretion disc is consistent with part of the optical variability of NGC 4395 but it cannot explain all of the variability. At least one other source of variations is needed, particularly at low frequencies, but the physical origin of such variations is, as yet, unknown.

ACKNOWLEDGEMENTS

MWJB acknowledges support from the UK Science and Technology Facilities Council (STFC) in the form of studentship ST/S505705/1. IMcH and DK acknowledge support from STFC from grant ST/V001000/1. VSD acknowledges support from STFC from grant ST/Z000033/1. EMC acknowledges support from NSF under grant AST-1909199. JVHS acknowledges support from STFC grant ST/V000861/1. JHK acknowledges grant PID2022-136505NB-I00 funded by MCIN/AEI/10.13039/501100011033 and also the European Regional Development Fund (MSCA EDUCADO, GA 101119830).

This paper is based on observations by a number of ground-based telescopes, i.e. the Liverpool Telescope (LT), the Las Cumbres Observatory global telescope network (LCOGT), the Gran Telescopio Canarias (GTC), the Zowada observatory, the Zwicky Transient Facility (ZTF), and also on observations by the NASA *Transiting Exoplanet Survey Satellite (TESS)*.

Both the LT and the GTC are installed at the Spanish Observatorio del Roque de los Muchachos of the Instituto de Astrofisica de Canarias on the island of La Palma. The LT is operated by Liverpool John Moores University with financial support from STFC. LCOGT is a non-profit organization based in California which runs a network of telescopes around the globe. The Zowada observatory is run by Wayne State University, Michigan. The ZTF is a wide-field survey monitoring facility based at the Palomar Observatory, California.

DATA AVAILABILITY

The data underlying this article will be shared on reasonable request to the corresponding author.

REFERENCES

Arevalo P., Uttley P., 2006, MNRAS, 367, 801

Arévalo P., Uttley P., Kaspi S., Breedt E., Lira P., McHardy I. M., 2008, MNRAS, 389, 1479

Arévalo P., Uttley P., Lira P., Breedt E., McHardy I. M., Churazov E., 2009, MNRAS, 397, 2004

Borucki W. J. et al., 2010, Science, 327, 977

Breedt E., 2010, PhD thesis, Physics and Astronomy, Univ. Southampton Breedt E. et al., 2009, MNRAS, 394, 427

Breedt E. et al., 2010, MNRAS, 403, 605

Brown T. M. et al., 2013, PASP, 125, 1031

Burke C. J., Shen Y., Chen Y.-C., Scaringi S., Faucher-Giguere C.-A., Liu X., Yang Q., 2020, ApJ, 899, 136

Burke C. J. et al., 2021, Science, 373, 789

```
Cameron D. T., McHardy I., Dwelly T., Breedt E., Uttley P., Lira P., Arevalo
   P., 2012, MNRAS, 422, 902
Carr R., Cinabro D., Cackett E., Moutard D., Carroll R., 2022, PASP, 134,
Cho H. et al., 2021, ApJ, 921, 98
Connolly S. D., 2015, preprint (arXiv:1503.06676)
Czerny B., Schwarzenberg-Czerny A., Loska Z., 1999, MNRAS, 303, 148
Deeming T. J., 1975, Ap&SS, 36, 137
den Brok M. et al., 2015, ApJ, 809, 101
Dhillon V. S. et al., 2021, MNRAS, 507, 350
Edelson R., Vaughan S., Malkan M., Kelly B. C., Smith K. L., Boyd P. T.,
   Mushotzky R., 2014, ApJ, 795, 2
Edelson R. et al., 2015, ApJ, 806, 129
Edelson R., Gelbord J., Cackett E., Peterson B. M., 2019, ApJ, 870, 123
Edri H., Rafter S. E., Chelouche D., Kaspi S., Behar E., 2012, ApJ, 756, 73
Elvis M., 2000, ApJ, 545, 63
Emmanoulopoulos D., Papadakis I. E., Nicastro F., McHardy I. M., 2013,
   MNRAS, 429, 3439
Hagen S., Done C., 2023, MNRAS, 521, 251
Hagen S., Done C., Edelson R., 2024, MNRAS, 530, 4850
Horne K., Peterson B. M., Collier S. J., Netzer H., 2004, PASP, 116, 465
Kammoun E. S., Dovciak M., Papadakis I. E., Caballero-Garcia M. D., Karas
    V., 2021, ApJ, 907, 20
Kara E. et al., 2021, ApJ, 922, 151
Kelly B. C., Bechtold J., Siemiginowska A., 2009, ApJ, 698, 895
Kelly B. C., Becker A. C., Sobolewska M., Siemiginowska A., Uttley P.,
   2014, ApJ, 788, 33
Korista K. T., Goad M. R., 2001, ApJ, 553, 695
Korista K. T., Goad M. R., 2019, MNRAS, 489, 5284
Lawrence A., Watson M. G., Pounds K. A., Elvis M., 1987, Nature, 325, 694
Lewin C., Kara E., Cackett E. M., Wilkins D., Panagiotou C., García J. A.,
   Gelbord J., 2023, ApJ, 954, 33
Masci F. J. et al., 2018, PASP, 131, 018003
McHardy I., Czerny B., 1987, Nature, 325, 696
McHardy I. M., 1988, Mem. Soc. Astron. Ital., 59, 239
McHardy I. M., Papadakis I. E., Uttley P., Page M. J., Mason K. O., 2004,
   MNRAS, 348, 783
McHardy I. M., Koerding E., Knigge C., Uttley P., Fender R. P., 2006, Nature,
   444, 730
McHardy I. M. et al., 2014, MNRAS, 444, 1469
McHardy I. M. et al., 2016, Astron. Nachr., 337, 500
McHardy I. M. et al., 2018, MNRAS, 480, 2881
McHardy I. M. et al., 2023, MNRAS, 519, 3366
Montano J. W., Guo H., Barth A. J., U V., Remigio R., González-Buitrago D.
   H., Hernández Santisteban J. V., 2022, ApJ, 934, L37
Mushotzky R. F., Edelson R., Baumgartner W., Gandhi P., 2011, ApJ, 743,
   L12
Nandra K., Papadakis I. E., 2001, ApJ, 554, 710
Netzer H., 2019, MNRAS, 488, 5185
Neustadt J. M. M., Kochanek C. S., 2022, MNRAS, 513, 1046
Nolan P. L. et al., 1981, ApJ, 246, 494
Panagiotou C., Papadakis I., Kara E., Kammoun E., Dovčiak M., 2022, ApJ,
   935, 93
Peterson B. M. et al., 2005, ApJ, 632, 799
Ponti G., Papadakis I., Bianchi S., Guainazzi M., Matt G., Uttley P., Bonilla
   N. F., 2012, A&A, 542, A83
Ricker G. R. et al., 2014, in Oschmann J. M. J., Clampin M., Fazio G. G.,
   MacEwen H. A., eds, Proc. SPIE Conf. Ser. Vol. 9143, Space Telescopes
   and Instrumentation 2014: Optical, Infrared, and Millimeter Wave. SPIE,
   Bellingham, p. 914320
Serafinelli R. et al., 2024, A&A, 690, A145
Shappee B. J. et al., 2014, ApJ, 788, 48
Simm T. et al., 2015, A&A, 584, A106
```

Cackett E. M., Horne K., Winkler H., 2007, MNRAS, 380, 669

Cackett E. M., Zoghbi A., Ulrich O., 2022, ApJ, 925, 29

Korista K., 2018, ApJ, 857, 53

Cackett E. M. et al., 2020, ApJ, 896, 1

Cackett E., Chiang C.-Y., McHardy I., Edelson R., Goad M., Horne K.,

Simm T., Salvato M., Saglia R., Ponti G., Lanzuisi G., Trakhtenbrot B., Nandra K., Bender R., 2016, A&A, 585, A129

Smith K. L., Mushotzky R. F., Boyd P. T., Malkan M., Howell S. B., Gelino D. M., 2018, ApJ, 857, 141

Steele I. A. et al., 2004, in Oschmann Jacobus M., Jr., ed, Proc. SPIE Conf. Ser. Vol. 5489, The Liverpool Telescope: Performance and First Results. SPIE, Bellingham, p. 679

Stone Z., Shen Y., 2023, MNRAS, 524, 4521

Stone Z. et al., 2022, MNRAS, 514, 164

Summons D. P., 2007, PhD thesis, Univ. Southampton

Timmer J., König M., 1995, A&A, 300, 707

Tortosa A. et al., 2023, MNRAS, 526, 1687

Uttley P., McHardy I. M., Papadakis I. E., 2002, MNRAS, 332, 231

Uttley P., Edelson R., McHardy I. M., Peterson B. M., Markowitz A., 2003, ApJ, 584, L53 Vaughan S., Iwasawa K., Fabian A. C., Hayashida K., 2005, MNRAS, 356, 524

Vincentelli F. M. et al., 2021, MNRAS, 504, 4337

Vincentelli F. M., McHardy I., Hernandez Santisteban J. V., Cackett E. M., Gelbord J., Horne K., Miller J. A., Lobban A., 2022, MNRAS, 512, L33

Woo J.-H., Cho H., Gallo E., Hodges-Kluck E., Le H. A. N., Shin J., Son D., Horst J. C., 2019, Nat. Astron., 3, 755

Yu W., Richards G. T., Vogeley M. S., Moreno J., Graham M. J., 2022, ApJ, 936, 132

Zu Y., Kochanek C. S., Kozłowski S., Udalski A., 2013, ApJ, 765, 106

This paper has been typeset from a $T_EX/I \Delta T_EX$ file prepared by the author.